Carbon Energy

WILEY

CARBON ENERGY

RESEARCH ARTICLE OPEN ACCESS

New Zeolitic Imidazolate Framework-Derived N-Doped Carbon LiCl Composites for Sorption Thermal Batteries Utilizing Solar Energy

Jan Marčec[1,2] | Marija Švegovec[1,2] | Matjaž Mazaj[1] | Andraž Krajnc[1] | Boštjan Genorio[3] | Daniel Lager[4] | Nataša Zabukovec Logar[1,2] | Alenka Ristić[1]

[1]National Institute of Chemistry, Ljubljana, Slovenia | [2]School of Science, University of Nova Gorica, Nova Gorica, Slovenia | [3]Faculty of Chemistry and Chemical Technology, University of Ljubljana, Ljubljana, Slovenia | [4]Energy Department, Sustainable Thermal Energy Systems, Austrian Institute of Technology GmbH, Vienna, Austria

Correspondence: Alenka Ristić (alenka.ristic@ki.si)

Received: 28 October 2025 | **Revised:** 26 February 2026 | **Accepted:** 25 March 2026

Keywords: amorphous hierarchical carbon | LiCl composites | solar energy | sorption thermal battery | water sorption

ABSTRACT

The potential of sorption thermal batteries utilizing solar energy is increasingly recognized, but developing cost-effective, stable, and high-performance storage materials remains a major challenge. Here, we demonstrate for the first time the use of zeolitic imidazolate framework (ZIF)-derived nitrogen-doped carbons (ZDCs) as hosts for LiCl-embedded water sorbent composites. ZIF-90 and ZIF-94 were synthesized in acetone–water solvent mixtures and subsequently pyrolyzed at 950°C in argon to obtain N-doped disordered carbons with specific surface areas up to 842 $m^2 g^{-1}$, hierarchical porosity, and maximal water adsorption capacity of up to 0.69 $g g^{-1}$. The structural features of the carbons were elucidated by transmission electron microscopy, X-ray photoelectron spectroscopy, Raman, and solid-state nuclear magnetic resonance spectroscopy. The composites with LiCl, prepared via incipient wetness impregnation, exhibited excellent cycling stability and showed no deliquescence or decrease in water uptake over 50 cycles under adsorption at 30°C, desorption at 120°C, and condensation/evaporation at 10°C. Remarkably, under these conditions, an energy storage density of 966.9 kWh m^{-3} can be achieved. These results show that ZDC-LiCl composites represent a promising class of stable, high-performance materials for efficient sorption thermal batteries.

1 | Introduction

Solar energy is considered one of the most promising candidates for the green transition and the abandonment of fossil fuels. To overcome the discrepancy between energy generated by renewables and actual energy demand, thermal energy storage technology is a key factor, as it is an economical storage solution that efficiently utilizes solar renewable energy and waste heat, offering a wide range of storage options (sensible, latent, and thermochemical) for different storage periods. Thermochemical heat storage (TCHS) has gained more attention in recent years, as it provides the highest energy density and no heat losses over time compared to sensible and latent heat storage. TCHS is also represented by the sorption thermal battery (STB) [1, 2], a technology based on reversible charging/desorption (endothermic process) and discharging/adsorption (exothermic process) of a material. During the charging process (Supporting Information S1: Figure S1), the system is heated by an external heat source (e.g., solar collector) to desorb the sorbate from the surface of the sorbent. In the discharge step, the sorbate is adsorbed onto the surface of the sorbent, releasing heat. The generated heat can be used, for example, for domestic water and space heating.

The efficiency of this technology is determined by the performance of the sorbents used, which is related to their structural properties and preparation procedures [3]. The selection of sorbent materials is a crucial step in STB, as it influences the adsorption capacity and

overall heat storage capacity. Hence, optimal sorbents should have high sorption capacity, thermal and chemical stability, adequate structural characteristics, low desorption temperatures when used with evacuated tube collectors (80°C–120°C), non-toxicity, good hydrothermal stability over multiple cycles, and no hysteresis in the adsorption and desorption curves during sorption cycles [4]. Due to these requirements, thermally stable nanoporous materials such as zeolites, aluminophosphates, metal-organic frameworks (MOFs), and composites of confined hygroscopic salt hydrates in porous matrices have been considered suitable candidates for STB [5]. Hygroscopic salt hydrates (halides, sulfates, nitrates, and bromides) release a high amount of heat during hydration. For example, lithium chloride (LiCl) confined in silica gel exhibits suitable properties for use in low-temperature (solar) STB ($T_{charging} < 120°C$), such as high water capacity at low relative humidity (RH), and high energy storage density ($> 180\ kWh\ m^{-3}$) [6], to name some of them. However, the main drawbacks of using hydrated salts as thermochemical materials (TCMs) are poor cyclic stability, slow kinetics, deliquescence, agglomeration, swelling, and corrosion. These drawbacks have led to combining them with the porous matrix, which finely distributes the salt across the surface, decreases particle size, affects the state and properties of the salt, and facilitates mass and heat transport through the solid. The sorption properties of the composites can be tailored by varying the chemical nature, amount, and particle size of the incorporated salt and, on the other hand, depend strongly on the structural (pore size/shape/volume) and hydrophilic properties of the porous host matrix, as well as host–salt interactions. Carbonaceous materials such as multiwall carbon nanotubes (MWCNTs) [7], graphene oxide [8], expanded graphite [9], aerogel [10], and MOF-derived carbon [11] have been used as matrices due to their high porosity, large surface area, and high thermal conductivity, although they exhibit low water adsorption capacity at low RH. Zeolitic imidazolate framework (ZIF)-derived carbons (ZDCs) are a group of N-doped carbonaceous materials prepared by pyrolysis of ZIF at high temperatures (600°C–1200°C) in an inert atmosphere (N_2 or Ar) [12], making them suitable as supports or active components in catalysis, adsorption, and energy-related applications. The properties of ZDCs can be tuned by preparing precursor ZIFs with different functional groups (e.g., methyl and carbaldehyde) and topologies. ZDC-8, a ZIF-8-derived compound, has been explored for water adsorption and thermochemical energy storage by Yuan et al. [13]. They found that non-activated samples exhibited water uptake at lower relative pressures ($p\ p_0^{-1} < 0.4$) due to the presence of pyrrolic and pyridinic nitrogen groups, which strongly polarize the carbon surface and enhance hydrophilicity. Yang et al. reported the preparation of ZDC-8 composites with varying LiOH content, showing that increasing the LiOH content led to increased water adsorption [11]. This research significantly advanced the development of ZDCs for sorption-based thermal batteries.

In this study, we report a facile and straightforward preparation of new ZIF-derived N-doped carbons, ZDC-90 and ZDC-94, and their composites with LiCl for low-temperature (solar) sorption heat storage. ZIF-90 [14] and ZIF-94 were selected as precursors due to their simple, green synthesis and advantageous structural and morphological properties. Both ZIF-90 and ZIF-94 exhibit hydrophilic properties due to carbaldehyde functional groups in their structures. Moreover, for the first time, ZIF-94 is synthesized using acetone and water as solvents. These ZIFs exhibit high specific surface areas (SSA), good thermal stability, phase purity, and low thermal conductivity, which can be addressed by producing ZDCs. As such, the proposed ZDCs hold great promise as matrices for LiCl and as efficient STB composites for space heating under working conditions such as an adsorption temperature of 30°C, a desorption temperature of 120°C, and a condensation/evaporation temperature of 10°C, storing solar energy up to $967\ kWh\ m^{-3}$.

2 | Results and Discussion

2.1 | Synthesis and Structural Properties of ZIF-90 and ZIF-94

Pure ZIF-90 and ZIF-94 were successfully synthesized from the acetone–water solution at ambient pressure and 60°C, as confirmed by powder X-ray diffraction (PXRD) (Supporting Information S1: Figure S2), Fourier transform infrared (FTIR) (Supporting Information S1: Figure S3), and scanning electron microscopy (SEM) (Supporting Information S1: Figure S4), showing a dodecahedral shape characteristic of the SOD topology, with non-uniform particle sizes ranging from 500 nm to 2 μm. The use of acetone and water resulted in the formation of a pure ZIF-94 phase, avoiding hazardous solvents such as DMF and THF (Supporting Information S1: Table S2). Because acetone and water were used, the activation step could be omitted, reducing the overall cost of ZIF-94 synthesis. Furthermore, ZIF-94 with hierarchical porosity and high SSA was obtained.

The detailed experimental information is provided in the Supporting Information. Both samples exhibit hierarchical features with micropores and mesopores (Supporting Information S1: Figure S5), resulting from the synthesis procedure. The ZIFs have high SSA (Supporting Information S1: Table S2), making the acetone–water solvent advantageous for synthesis. Furthermore, acetone can be recycled after synthesis, aligning with the principles of sustainable approaches.

2.2 | Synthesis and Structural Properties of ZDC-90 and ZDC-94

ZDCs were prepared by pyrolysis of precursors ZIF-90 and ZIF-94 in an argon atmosphere at 950°C. Figure 1A shows the PXRD patterns of the ZDCs with two broad diffraction peaks at approximately 25° and 44°, corresponding to the (0 0 2) and (1 0 0) planes in a non-graphitic disordered carbon structure, respectively [15]. The disappearance of the characteristic peaks from the crystalline precursor (Supporting Information S1: Figure S2) indicates complete transformation into amorphous carbonaceous materials. Additionally, no diffraction peaks assigned to ZnO are observed. Raman spectroscopy, as one of the most commonly used techniques to study the chemical structure and disorder of carbonaceous materials, reveals in Figure 1B two characteristic peaks at ~1350 and ~1590 cm^{-1} corresponding to the D band (structural defects) and G band (graphitic phase of carbon), respectively [16]. A shoulder between 1400 and 1450 cm^{-1} can be seen, which can be assigned to the presence of nitrogen in the structure of both ZDCs [17]. The 2D band [18] is not observed in ZDC-94, indicating the presence of more defects in the carbon structure. To estimate the degree of defects in ZDCs, the intensity of D and G

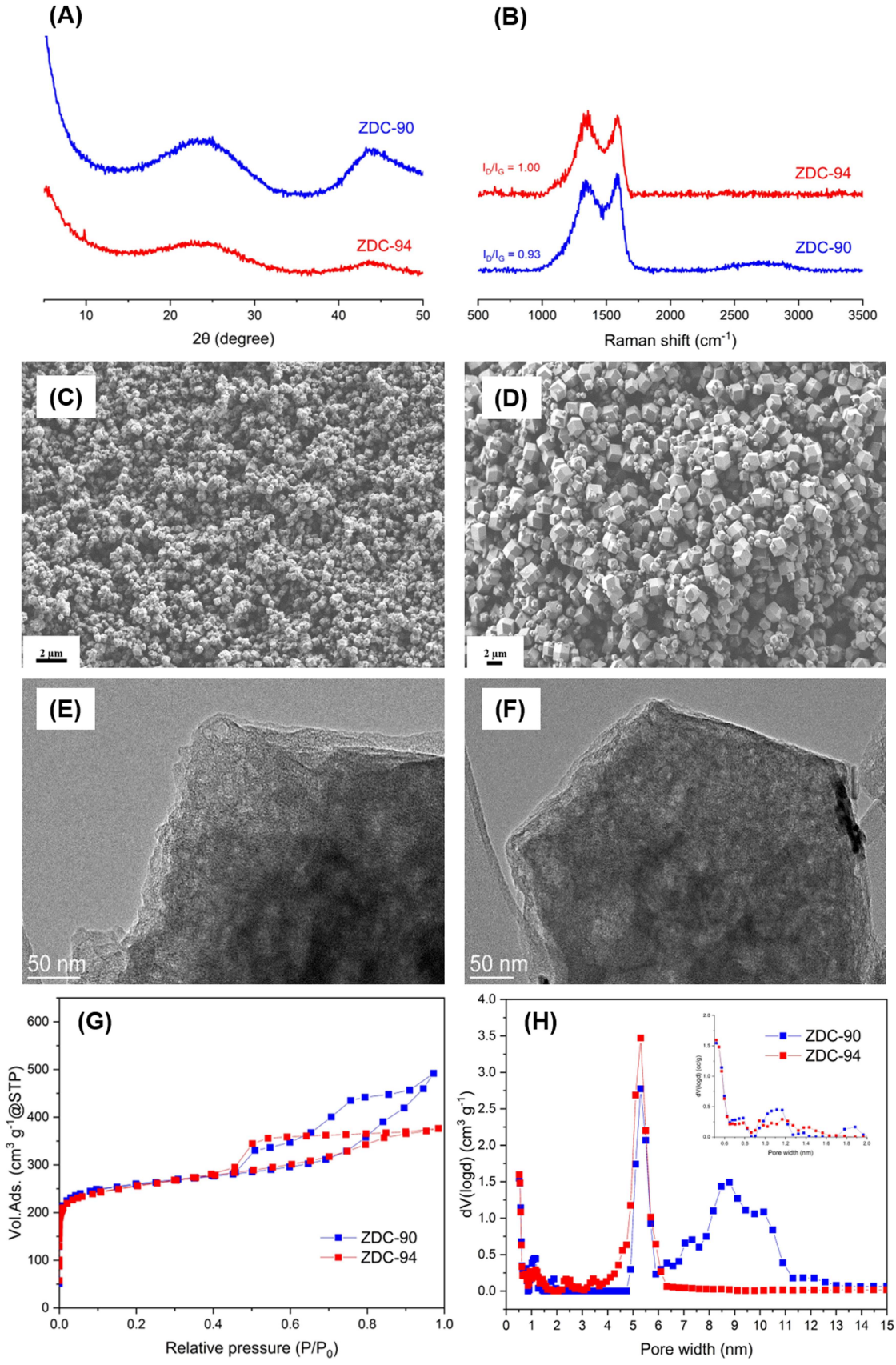

FIGURE 1 | (A) PXRD patterns of ZDC-90 and ZDC-94, (B) Raman spectra of ZDC-90 and ZDC-94, (C, D) SEM images of ZDC-90 and ZDC-94, respectively, (E, F) TEM images of ZDC-90 and ZDC-94, respectively, (G) nitrogen sorption isotherms of ZDC-90 and ZDC-94 at 77 K, and (H) pore size distributions of ZDC-90 and ZDC-94 using NLDFT algorithm.

peaks in Raman spectra was compared, showing values of 0.93 for ZDC-90 and 1.00 for ZDC-94, additionally confirming the generation of more defects in ZDC-94 [19]. SEM (Figure 1C,D) and TEM (Figure 1E,F) measurements were performed to elucidate the morphology and nanostructure of the ZDCs. Both ZDC-90 and ZDC-94 retain the dodecahedral particle morphologies and sizes of their ZIF precursors, demonstrating that the overall particle shape is preserved during pyrolysis. TEM imaging further reveals that the ZDCs possess highly disordered nanoporous structures [20], which is typical for carbons derived from ZIFs, and suggests the coexistence of micropores and mesopores, arising from the removal of organic linkers and the collapse of the framework upon pyrolysis. These morphological and nanostructural features are expected to strongly influence sorption performance, as particle size affects diffusion pathways while the disordered porous network provides accessible adsorption sites. To gain insight into the structural properties, nitrogen physisorption experiments at 77 K were performed (Figure 1G). Both ZDCs display mixed Type I/IV isotherms, confirming the presence of micro- and mesopores. SSA are 842 $m^2 g^{-1}$ for ZDC-90 and 833 $m^2 g^{-1}$ for ZDC-94. Compared to their precursors, SSA of ZDC-90 show a decrease from 1250 $m^2 g^{-1}$, while the SSA of ZDC-94 increases from 618 to 833 $m^2 g^{-1}$ after pyrolysis (Supporting Information S1: Table S4). ZDC-90 exhibits an H5 hysteresis loop, often associated with plugged pores, possibly from ZnO migration during pyrolysis and/or microporous plugs [21–23]. In contrast, ZDC-94 shows an H4 hysteresis loop, characteristic of slit-like mesopores [24], as also reported for activated carbons and N-enriched mesoporous carbons [25]. Similar H4 behavior has been observed in carbons from Norit [26], ZDC-9 prepared at 800°C [27], and ZDC-7 synthesized under Ar at 950°C (SSA 406 $m^2 g^{-1}$) [28]. The pore size distribution curves (Figure 1H) of ZDC-90, analyzed by the nonlocal density functional theory (NLDFT) algorithm, exhibited micropores (Figure 1H, inset) centered at 0.52, 0.75, 1.1, and 1.8 nm, as well as mesopores around 5.4 nm and a broad distribution from 6 to 14 nm. A slightly different pore size distribution can be observed for ZDC-94, showing micropores at 0.52, 0.75, 0.94, 1.17, and 1.43 nm and mesopores at 2.4, 3.4, and 5.3 nm. These findings suggest that the pore arrangement of the ZIF precursors (Supporting Information S1: Figure S5), in addition to particle size (500 nm to 2 μm, Supporting Information S1: Figure S4), also influences the resulting carbon's pore architecture, confirming the hierarchical pore nature. High-temperature treatment of ZIFs in an inert atmosphere preserves the hierarchical porous structure, which is advantageous for composite formation, as shown by Ristić et al. [29].

Both ZDCs are thermally stable up to 380°C in air (Supporting Information S1: Figure S6). X-ray photoelectron spectroscopy (XPS) analysis was performed to gain deeper insights into the surface composition of the ZDCs. The XPS survey spectra (Supporting Information S1: Figure S7A) show the presence of C, O, N, and Zn, with Zn content in both ZDCs around 1.7 at.%, which is slightly higher than the bulk energy dispersive X-ray spectroscopy results (Supporting Information S1: Table S3). The binding energy difference between the Zn 2p3 and Zn 2p1peaks is approximately 23 eV, indicating the presence of Zn^{2+}, suggesting that although the pyrolysis temperature exceeded the sublimation temperature of ZnO (905°C), a small amount of ZnO remains in the structure. This amount of ZnO is not expected to affect the STB performance; therefore, the use of additional harsh chemicals can be avoided. Supporting Information S1: Figure S7B–G show the high-resolution C 1s, O 1s, and N 1s spectra of the ZDCs. Nitrogen functional groups carry partial electrostatic charges, influencing water adsorption [30]. The deconvoluted N 1s spectra (Supporting Information S1: Figure S7D,G) reveal four characteristic peaks for both ZDCs. The peak between 400 and 401 eV corresponds to graphitic nitrogen bonded to three carbon atoms [31]. Peaks in the 397–398 eV and 398–399 eV ranges are attributed to pyridinic and pyrrolic nitrogen, respectively. These groups have been shown to influence water adsorption at low partial pressures [13]. The atomic percentages of N species are summarized in Table 1, showing similar pyrrolic and graphitic nitrogen content, while ZDC-90 contains a higher amount of pyridinic nitrogen and a lower amount of oxidized nitrogen compared to ZDC-94. The C 1s spectra (Supporting Information S1: Figure S7B,E) can be deconvoluted into five peaks at ~284, 285, 286, 288, and 288.5 eV corresponding to sp^2 C, sp^3 C, C—O, C=O, and O=C—O, respectively [32, 33]. The peak at 286 eV also corresponds to C—N, signifying successful nitrogen incorporation [32]. The O 1s spectra (Supporting Information S1: Figure S7C,F) reveal the presence of oxygenated carbon species and traces of ZnO, even though ZnO is not detected by PXRD.

2.3 | Structural and Thermophysical Properties of Composites

The composites were prepared using incipient wetness impregnation (IWI) in order to eliminate additional washing steps to remove excess surface salt [34]. With this method, the volume of salt solution used for composite preparation matches the pore volume of the matrix. This approach promotes pore filling via capillary forces, resulting in a product that is subsequently dried at room temperature to ensure the pore filling and to prevent agglomeration of salt particles on the external surface of the matrix, as confirmed by PXRD. LiCl is mainly confined within the micropores of ZDCS, with sizes up to 1 nm, and partly within mesopores, which are arranged in a disordered manner. The partial occupancy and disorder of the mesopores allow water to access and react with the salt. Therefore, the IWI method is advantageous for the composite preparation. The composites were labeled ZDC-x-Liy (where x indicates the ZIF precursor and y indicates the Li content; for example, ZDC-

TABLE 1 | Nitrogen species composition in ZDCs.

Sample	Pyridinic-N (at.%)	Pyrrolic-N (at.%)	Graphitic-N (at.%)	Oxidized-N (at.%)
ZDC-90	22.3	33.8	32.9	12.0
ZDC-94	17.8	34.9	31.7	15.7

90-Li10, as shown in Supporting Information S1: Table S1). PXRD patterns of the ZDC composites with LiCl (Figure 2A,B) show broad peaks at approximately 25° and 45° 2θ, similar to the pristine ZDCs. The absence of additional LiCl diffraction peaks suggests that the salt is well dispersed and confined within the pores of the ZDCs.

The selection of an appropriate matrix is critical for achieving high water sorption capacity and energy storage density. In the microporous materials, salt can block the pores, impeding mass transport. Therefore, a matrix with a hierarchical structure, comprising both micro- and mesopores, is essential to mitigate these limitations. Although MOFs have also been investigated for composite formation [34, 35], care must be taken as hygroscopic salts, particularly chlorides, can degrade the MOF structure. ZDCs are thus suitable candidates due to their hierarchical porosity and favorable thermophysical properties (see below). Supporting Information S1: Table S4 presents the SSA, total pore volume (V_{tot}), micropore volume (V_{mic}), and mesopore volume (V_{mes}) values of the precursor ZIFs, ZDC matrices, and composites. As expected, increasing salt content leads to a significant decrease in SSA and total pore volumes [29]. LiCl is confined in micropores and mesopores in the matrices of the composites, showing typical tailing and widening of the hysteresis loops [29, 36]. Specifically, the composites of both ZDCs with higher salt contents (15 and 20 wt.%) show only the presence of mesopores (Figure 2C,D).

One of the requirements of TCMs to enhance the heat transport in the systems is adequate thermal conductivity [36]. The effective thermal conductivity was calculated based on the materials' thermal diffusivity, specific heat capacity, and density. Conventional nanoporous materials such as zeolites, silicas, and aluminophosphates typically exhibit low thermal conductivity values, ranging from 0.15 to 0.25 $W\,m^{-1}\,K^{-1}$ [37], while nanoporous carbons show even lower values of 0.10 $W\,m^{-1}\,K^{-1}$ due to their high porosity [38]. The pure ZDCs display higher thermal conductivity values of 0.58 and 0.81 $W\,m^{-1}K^{-1}$ for ZDC-94 and ZDC-90, respectively. These values are still lower than those of expanded graphite (up to 2 $W\,m^{-1}K^{-1}$), but higher than those of conventional nanoporous materials. ZDC-90-Li composites showed thermal conductivity from 0.338 to 0.536 $W\,m^{-1}\,K^{-1}$; similar values were determined for ZDC-94-Li composites (from 0.326 to 0.498 $W\,m^{-1}\,K^{-1}$). Variations in thermal conductivity may arise from the inherent complexity of measuring thermophysical properties in porous structures. The

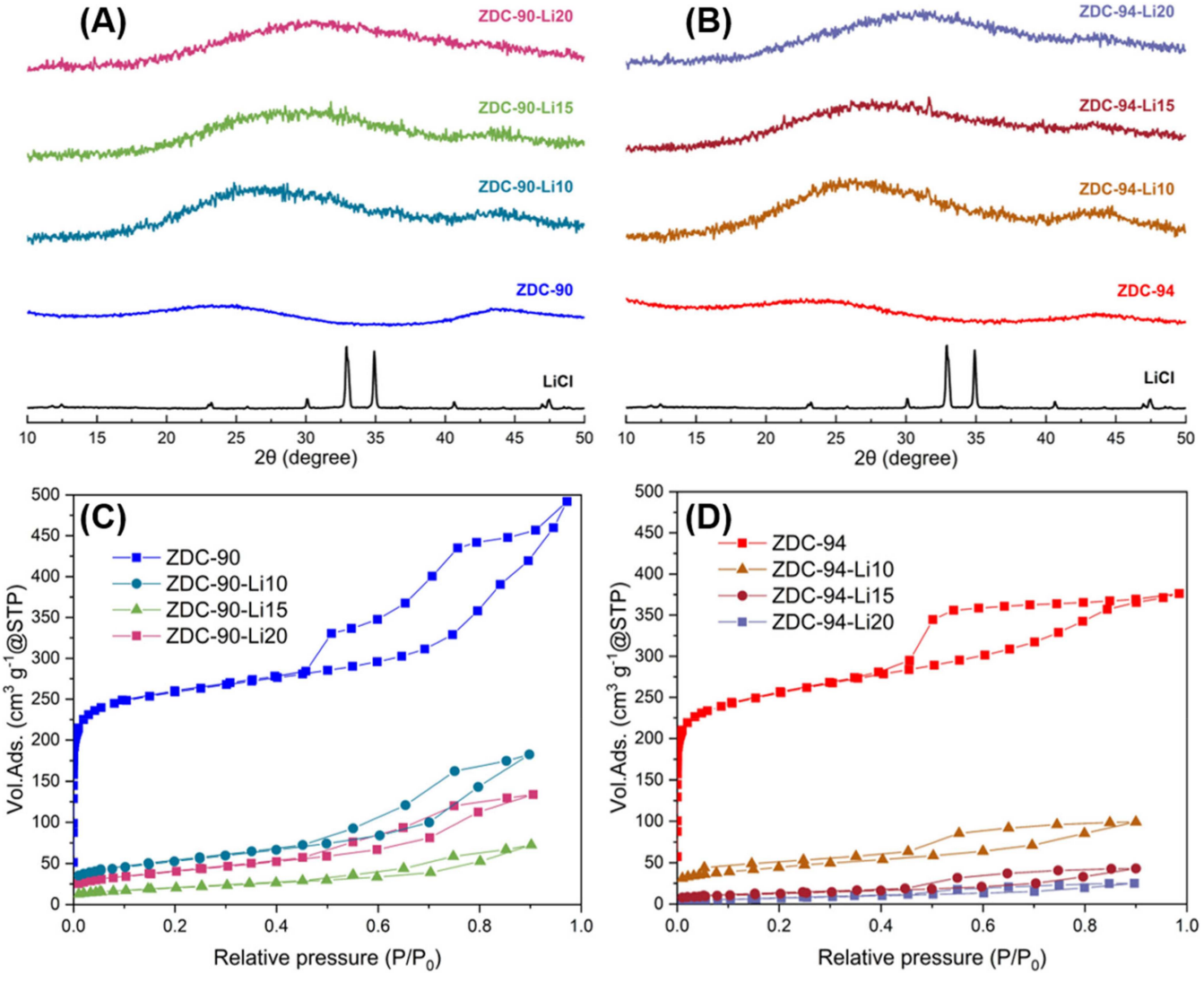

FIGURE 2 | (A, B) PXRD patterns of ZDCs and their composites, and (C, D) nitrogen physisorption at 77 K of ZDCs and their composites.

thermal conductivity of the composite of ZDC-8-LiOH, determined by hot disk, showed thermal conductivity of 0.79 W $m^{-1} K^{-1}$ [39]. The densities of the ZDCs and composites range from 1.664 to 2.131 g cm^{-3}.

2.4 | Water Sorption Properties

2.4.1 | *Water Adsorption on ZIF-90 and ZIF-94*

Water adsorption isotherms (Supporting Information S1: Figure S8A) of ZIF-90 and ZIF-94 exhibit a typical Type V shape, with a hydrophobic region from 0% RH to 25% RH, followed by an adsorption step between 25% RH and 40% RH. Water adsorption increases gradually up to 40% RH and then continues to rise slowly. The maximal water uptakes at 95% RH are 0.39 g g^{-1} for ZIF-90 [14] and 0.19 g g^{-1} for ZIF-94. At 30% RH, ZIF-94 shows a water uptake of 0.13 g g^{-1}, while ZIF-90 has a lower uptake of 0.09 g g^{-1}. The presence of a hysteresis loop between 20% RH and 40% RH suggests capillary condensation within the pores of ZIF-90, while no hysteresis loop is observed in ZIF-94. Canivet et al. [40] investigated water adsorption on a series of MOFs, including ZIF-94. Their ZIF-94 sample, synthesized in DMF, exhibited a maximal water uptake of 0.15 g g^{-1} at 90% RH and approximately 0.07 g g^{-1} at 30% RH. These values are lower than those observed in this study, which can be attributed to differences in the synthesis procedure and solvent used. Similarly, Gao et al. [41] analyzed water uptake of ZIF-94 at 25°C, also prepared in DMF, and reported a lower maximal water uptake of around 0.14 g g^{-1} at 90% RH and 0.08 g g^{-1} at 30% RH. To assess ZIF-94 hydrothermal stability, 20 cycles were performed at 30°C and 80% RH adsorption and 120°C desorption. Supporting Information S1: Figure S8B reveals that the ZIF-94 prepared in the water and acetone solvent mixture exhibits a very constant water uptake of 0.18 g g^{-1}. Moreover, the PXRD pattern (Supporting Information S1: Figure S9) shows that ZIF-94 retained its crystal structure after 20 cycles. While higher water uptake was observed for ZIF-90, after the 20th cycle, it decreased by 4.9%.

2.4.2 | *Water Adsorption on ZDCs and Their Composites*

Water adsorption in carbonaceous materials is complex due to the interplay of several factors, such as the concentration and type of functional groups, their location and distribution on the surface, the pore size distribution, and pore connectivity [30]. Water adsorption isotherms of ZDC-90 and ZDC-94 at 30°C are shown in Figure 3A. Both materials exhibit Type IV isotherms, characterized by low water uptake at RH below 20%, followed by a two-step increase between 20% RH and 40% RH and above 70% RH, which is especially pronounced in ZDC-90. ZDC-90 shows a higher maximum water uptake of 0.67 g g^{-1} compared to 0.49 g g^{-1} for ZDC-94 at the same temperature, which can be related to different pore structures [30]. Both materials exhibit hysteresis loops due to capillary condensation [42]. Two distinct adsorption steps are evident in the water isotherm of ZDC-90. Similar behavior was reported by Horikawa et al. for resorcinol–formaldehyde cryogel-derived carbon [43]. The dual-step adsorption results from the initial adsorption of water molecules on functional nitrogen groups via hydrogen bonding, forming small water clusters. Once the clusters grow large enough, they enter the micropores. In contrast, larger clusters are required to access mesopores, leading to adsorption at higher RH levels. This phenomenon is more prominent in ZDC-90 due to its higher mesopore volume, as shown in Supporting Information S1: Table S4. Furthermore, the materials exhibit different types of hysteresis: ZDC-90 shows an H5 hysteresis loop, typical for materials with plugged mesopores, whereas ZDC-94 exhibits an H4-type hysteresis, indicative of slit-like mesopores [44]. Similarly, ZDC-94 also exhibits a two-step adsorption isotherm, but with a different desorption branch. Among other factors, the shape of the water sorption isotherm depends on the pore size distribution of the material. The pore sizes and arrangements of the ZDCs depend on the structural properties of the starting ZIF precursors. ZIF-90 exhibits a higher amount of mesopores compared to ZIF-94. Consequently, during pyrolysis, a greater amount of mesopores is formed in ZDC-90 than in ZDC-94, which affects the maximum water adsorption capacity. Both ZDC samples maintained the hierarchical pore

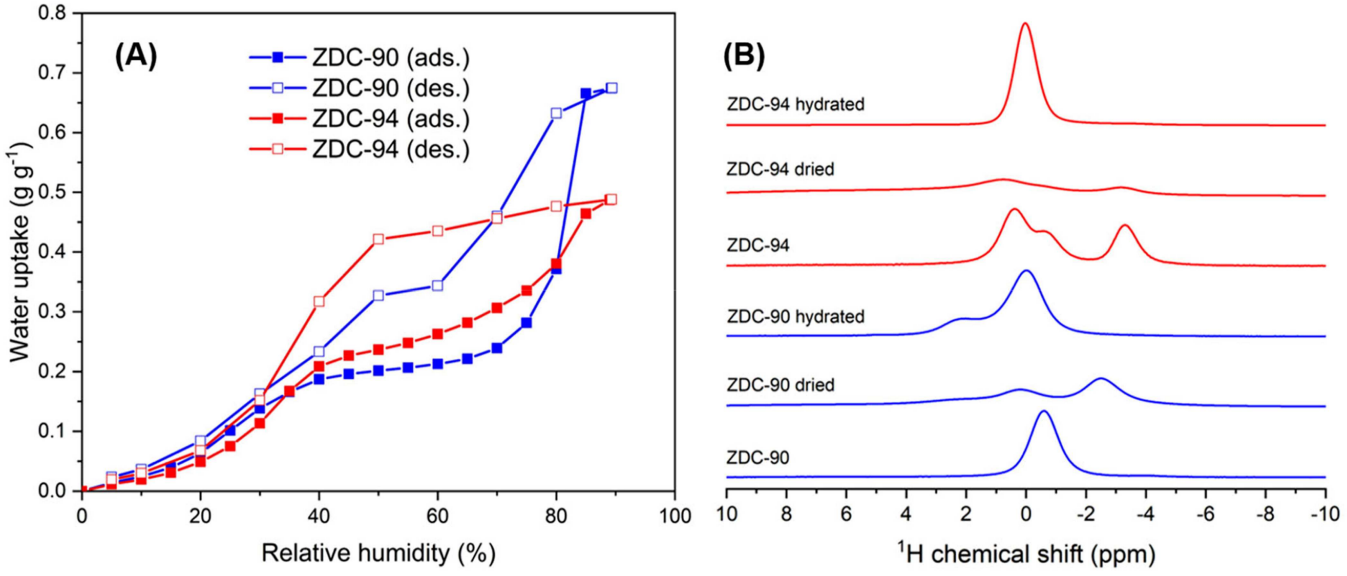

FIGURE 3 | (A) Water adsorption on ZDC-90 and ZDC-94 at 30°C and (B) ^{1}H MAS spectra of the as-received, dried, and hydrated ZDC-90 and ZDC-94.

arrangements of their ZIF precursors after pyrolysis. Yuan et al. systematically investigated water adsorption on ZDC-8 samples treated at various temperatures (700°C–1000°C), with and without HCl washing and KOH activation [13]. The non-activated ZDC-8 materials exhibit Type V water adsorption isotherms at 25°C, with water uptakes of 0.2, 0.16, 0.14, and 0.1 g g^{-1} at 30% RH for samples treated at 700°C, 800°C, 900°C, and 1000°C, respectively. In contrast, KOH-activated samples treated at 800°C and 1000°C show steep increases in water uptake only at higher p p_0^{-1} values, with negligible adsorption below 0.4 p p_0^{-1}. XPS analysis revealed a decrease in nitrogen content upon activation, which is believed to reduce water adsorption at low relative pressures. Similar results were shown by Lin et al. [45], who obtained water uptakes of 0.2 g g^{-1} at 25°C and 30% RH. However, when they prepared a mixed-linker MOF containing 2-methylimidazole and 3-methyl-1,2,4-triazole, pyrolyzed it at 650°C, and washed it with HCl, the resulting carbon showed a significant uptake improvement to 0.45 g g^{-1} under the same conditions. This implies that nitrogen content impacts water uptake at RH < 40%.

The role of nitrogen functional groups depends on their type, affinity toward water, concentration, and accessibility, which impacts the water uptake at RH < 40% [30, 43]. N-doped porous carbon enhances water adsorption through nitrogen functional groups such as pyridinic, pyrrolic, and graphitic nitrogen and nitrogen oxide species that boost surface polarity and affinity for polar molecules like water and improve hydrophilicity and adsorption sites [46]. Compared to undoped carbon, N-doping can increase water uptake by 20-50% under humid conditions due to hydrogen bonding with N sites according to Kumar et al. [46] and Wang et al. [47]. Specifically, pyridinic-N and pyrrolic-N functional groups have more affinity with water molecules than other N species [48–50]. Furthermore, these nitrogen functional groups are usually highly accessible, typically located on edges, defects, or within pores [43, 51]. Undoped carbons, such as activated carbons [52], as well as derived carbons from MOF-5 [53], CAU-10-H [54], and HKUST-1 [55], reveal a hydrophobic character of the carbon with a Type III/Type V isotherm shape [30]. Commercial activated carbon showed low water uptake (< 0.05 g g^{-1}) until 60% RH [52]. The water uptake of MOF-5-derived carbon at 30% RH was around 0.02 g g^{-1} [53], while CAU-10-H and HKUST-1-derived carbons showed water uptake of 0.15 g g^{-1} at 40% RH and 0.13 g g^{-1} at 50% RH, respectively [54, 55]. Investigations of Yuan et al. [13] suggest that water uptake of ZDC-8 at < 20% RH is correlated with the nitrogen content. ZDC-90 and ZDC-94 contain around 6.0% of nitrogen, showing three-times higher water uptake at 20% RH in comparison to ZDC-8 prepared at 900°C [49], which has 3.67% of nitrogen. In the case of our ZDCs, higher water uptakes at < 40% RH are reported compared to undoped MOF-derived carbons, which again indicates that nitrogen functional groups play a crucial role in water adsorption. More than 50% of nitrogen sites with more affinity for water are present in ZDC-90 and ZDC-94 (Table 1). This can be observed from the water sorption isotherms (Figure 3A), where the adsorption takes place already at 10% RH with low uptakes, and is increasing with the RH (0.2 g g^{-1} at 40% RH).

Solid-state ^{1}H MAS NMR spectra (Figure 3B) of ZDC-94 display several distinct water environments, reflecting strong confinement and a diverse surface. The most shielded resonance at −3.30 ppm arises from water in micropores directly adjacent to sp^2 carbon walls, where strong π-ring currents shift the signal far upfield [56]. Such strongly confined water is expected to exhibit high binding strength, which contributes significantly to the overall heat released upon adsorption but also requires higher temperature or longer time for desorption. A shoulder at −0.61 ppm corresponds to dynamically exchanging populations between wall and center sites, while the resonance at 0.30 ppm originates from more mobile pore water approaching bulk-like behavior [57]. This more weakly bound water is associated with faster desorption kinetics but a lower contribution to the adsorption enthalpy. Vacuum drying reduces but does not eliminate the micropore contribution (−3.20 ppm), indicating the persistence of strongly confined water, while rehydration at 75% RH collapses the spectrum into a dominant resonance near −0.01 ppm, reflecting rapid exchange across pore sites. Only a faint micropore contribution remains (−3.40 ppm). The ^{13}C CP MAS spectra (Supporting Information S1: Figure S10A) confirm a framework dominated by sp^2 carbons (~125 ppm), with weaker signals from edge C–O (~55 ppm) and sp^3 carbons (~15 ppm) [58]. These edge-related contributions vanish under humid conditions, because rapidly mobile water protons suppress efficient polarization transfer. In contrast, the ZDC-90 proton spectrum is dominated by a sharp resonance at −0.50 ppm, assigned to mobile water interacting with sp^2 walls. Notably, the as-prepared ZDC-90 sample was not fully dried and shows both micropore-associated upfield signals (−2.4 ppm) and a resonance associated with mobile water. This suggests partial rearrangement of confined water upon drying but preservation of characteristic micropore environments. Upon rehydration at 75% RH, the water resonance sharpens and shifts to −0.01 ppm, evidencing fast exchange that averages the pore environments to near bulk values [59].

Importantly, an additional resonance at ~2.2 ppm appears, which we assign to water located in larger mesopores [60]. Water residing in such larger pores is less strongly confined and therefore desorbs more readily, contributing primarily to fast adsorption–desorption kinetics rather than to high heat release. Unlike ZDC-94, the ^{13}C CP MAS spectra of ZDC-90 consistently show only the sp^2 resonance (~125 ppm) with no detectable contributions from edge carbons. In all cases, the direct-excitation ^{13}C MAS spectra (Supporting Information S1: Figure S10B) show only the sp^2 carbon resonance. The dominance of this signal arises from the short T_1 of sp^2 carbons, while C–O and sp^3 sites with longer T_1 remain largely undetected. Together, these NMR results correlate directly with the determined pore sizes and water adsorption data. ZDC-94 exhibits stronger water confinement in micropores, giving rise to highly shifted resonances, while ZDC-90 shows enhanced mesoporosity, reflected in the appearance of an additional mesopore-associated signal at ~2.2 ppm.

Figure 4A,B display the water sorption−desorption isotherms at 30°C for LiCl confined in ZDC-90 and ZDC-94 composites. Incorporating hygroscopic LiCl into the ZDC matrix significantly enhances water uptake, particularly at low RH. Water uptake increases with higher salt content. The composites containing the highest amount of LiCl show the highest water uptake (0.69 g g^{-1} for both ZDC-90 and ZDC-94) at 30% RH. Similar results were reported for MIL-101(Cr) composites containing 33% and 51% LiCl, which showed water uptakes of

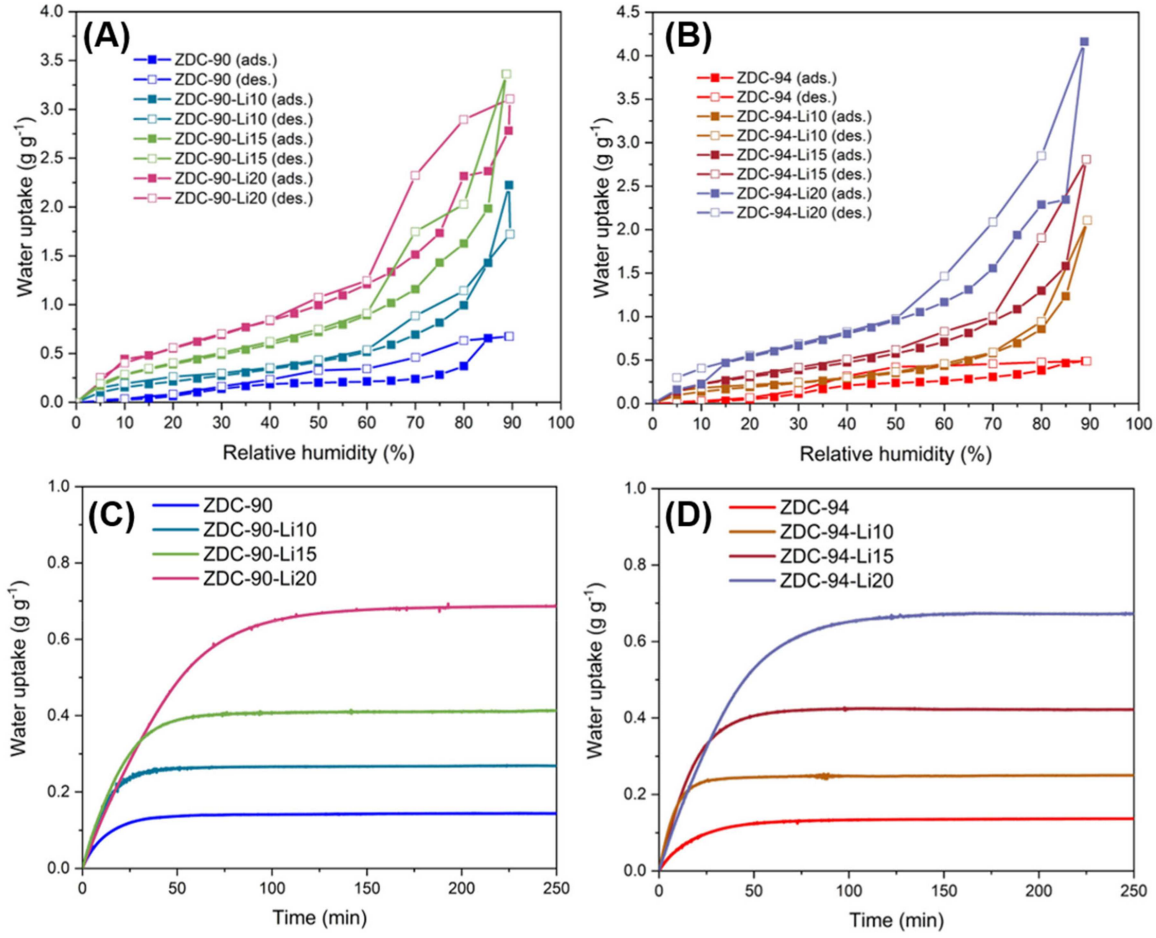

FIGURE 4 | (A, B) Water sorption−desorption isotherms at 30°C and (C, D) sorption kinetics at 30°C and 30% RH of ZDC-90-LiCl and ZDC-94-LiCl composites.

0.3 g g^{-1} and 0.8 g g^{-1}, respectively, at 30°C and 30% RH [61]. This enhancement is attributed to LiCl's high affinity for water at low RH. All composites exhibit hysteresis loops at high RH, with the loop becoming narrower as salt content decreases.

Water sorption kinetics were assessed using simultaneous thermogravimetric–differential scanning calorimetry (TG-DSC) connected to a water vapor generator at 30°C and 30% RH (Figure 4C,D). The results are in good agreement with those obtained using the gravimetric adsorption analyzer. The kinetic curves reveal rapid water adsorption for both pure ZDCs and their LiCl-containing composites.

ZDC-90 and ZDC-94 composites display similar adsorption behavior, indicating that at higher salt loadings, the matrix has minimal effect on overall water uptake. Among the samples, the composites Li10 and Li15, as well as the pure ZDCs, reach equilibrium within 60 min. However, the composites with the highest LiCl content exhibit slower adsorption kinetics, requiring up to twice as long to reach equilibrium. This delay is attributed to reduced diffusion rates due to salt agglomeration or pore blocking at higher salt contents.

2.5 | Sorption Heat Storage Determination

The heat of adsorption was determined using simultaneous TG-DSC under the working conditions for space heating as described in the introduction, by integrating the curves obtained from the DSC signal measured isothermally over time [62]. The experimentally determined values of energy storage capacity for the ZDC composites are shown in Figure 5A and Table 2. As observed, the heat of adsorption increases with LiCl content. The composites exhibit a consistent trend in water uptake and comparable heats of adsorption, further confirming that salt content is the dominant factor influencing the sorption performance of the materials. The highest energy storage capacity is observed for the composites containing the highest amount of LiCl, reaching nearly 2100 kJ kg^{-1} (Table 2). Notably, the composites labeled Li15, containing 15 wt.% LiCl, also show excellent performance, with values surpassing those commonly reported in the literature. Grekova et al. [7] used MWCNT as the matrix with 42 wt.% LiCl and polyvinyl alcohol as a binder to prepare a shaped composite. The composite showed a high heat storage capacity of 1700 kJ kg^{-1} under conditions of $T_{ads}/T_{des}/T_c = 35/65/15$°C. Similarly, Brancato et al. [63] used a similar composite with 55 wt.% of LiCl. They obtained a lower heat storage capacity of 1600 kJ kg^{-1} under $T_{ads}/T_{des}/T_c = 35/75/15$°C.

Table 2 shows water uptake and STB performance, supporting the potential of the proposed composites for further investigation at the pilot scale. The selected charging temperature of 120°C was chosen for integration with solar thermal collectors, making the system suitable for solar-assisted thermal energy storage applications [64, 65].

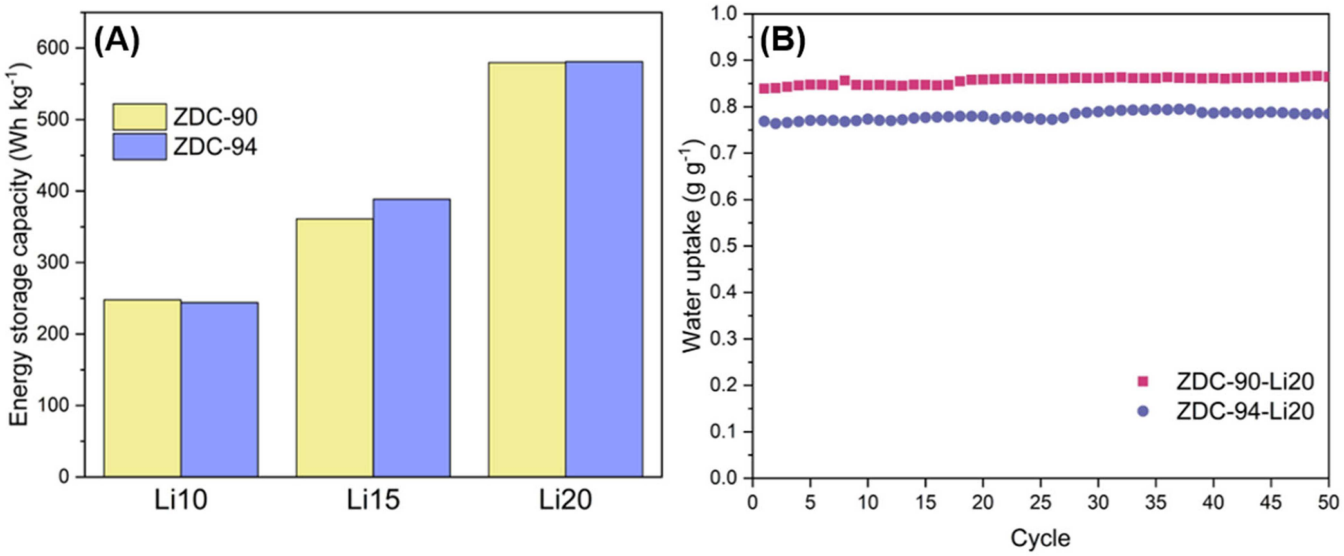

FIGURE 5 | (A) Energy storage capacity for the ZDC composites under working conditions $T_{ads}/T_{des}/T_{c/e} = 30/120/10°C$ and (B) hydrothermal stability of ZDC-90-Li20 (red) and ZDC-94-Li20 (blue) at adsorption temperature of 30°C and 40% RH and desorption temperature of 120°C.

TABLE 2 | Water adsorption uptake and determined energy storage densities for ZDC composites under the conditions $T_{ads}/T_{des}/T_{c/e} = 30/120/10°C$.

Sample	Water uptake ($g\ g^{-1}$)	Heat of adsorption ($kJ\ kg^{-1}$)	Energy storage capacity ($Wh\ kg^{-1}$)	Energy storage density ($kWh\ m^{-3}$)
ZDC-90	0.15	506.3	140.6	299.7
ZDC-90-Li10	0.27	892.5	247.9	426.7
ZDC-90-Li15	0.41	1299.8	361.0	597.9
ZDC-90-Li20	0.69	2086.9	579.7	957.7
ZDC-94	0.14	466.0	129.5	240.6
ZDC-94-Li10	0.25	878.3	244.0	412.3
ZDC-94-Li15	0.42	1399.2	388.7	646.7
ZDC-94-Li20	0.69	2091.9	581.1	966.9

Supporting Information S1: Table S5 shows the comparison of the heat of adsorption of LiCl composites prepared by other groups, as determined by DSC over time. As can be seen, the obtained heats of adsorption differ mainly depending on the experimental conditions used. The LiCl composites in the table exhibit lower heats of adsorption compared to the ZDC-LiCl composites.

2.6 | Hydrothermal Stability of ZDCs-Li20

The hydrothermal stability of the composites was evaluated using samples with 20 wt.% LiCl, as this represents the highest salt content and the greatest potential for salt leaching, over 50 sorption cycles (Figure 5B). It was reasoned that if these composites demonstrate stability, those with lower salt contents would likely perform as well or better. The cycling tests were conducted at an adsorption temperature of 30°C and 40% RH, followed by desorption at 120°C. The composite ZDC-90-20LiCl was also tested at lower desorption temperatures from 80°C to 90°C (Supporting Information S1: Figure S11), where flat plate solar collectors can be used. As shown in Figure 5B, the composite maintains stable water uptake over 50 cycles, with only minor variations observed, confirming its excellent hydrothermal (cycling) stability. Furthermore, elemental distribution analysis (Supporting Information S1: Figures S12 and S13) revealed no LiCl leakage from the matrix, most probably because the salt was predominantly trapped in the micropores.

3 | Conclusions

ZIF-derived carbons with disordered and hierarchical micro/mesostructures were successfully prepared for the first time from ZIF-90 and ZIF-94 precursors to confine LiCl for sorption thermal batteries for solar energy storage. Pyrolysis of the ZIF precursors at 950°C under an inert atmosphere yielded nitrogen-doped amorphous carbons. Because the pyrolysis temperature exceeded the evaporation point of ZnO, the resulting carbons did not require additional acid or base treatment, thus avoiding harsh chemicals. This approach produced amorphous nanoporous carbon materials with a high SSA of up

to 842 $m^2 g^{-1}$, a unique morphology derived from the precursor ZIFs, water adsorption imparted by the incorporated nitrogen atoms, hierarchical porosity, and a particular size of particles. XPS, Raman, and NMR analyses confirmed the presence of sp^2-hybridized carbon with additional defects, which were more pronounced in ZDC-94. Moreover, solid-state NMR analysis of hydrated ZDCs directly correlated with the determined pore sizes and water adsorption data. ZDC-94 exhibited stronger water confinement in micropores, resulting in highly shifted resonances, while ZDC-90 showed enhanced mesoporosity. The ZDCs demonstrated higher maximum water uptakes than their precursors: ZIF-90 and ZIF-94 achieved 0.39 and 0.19 $g g^{-1}$, while ZDC-90 and ZDC-94 reached 0.67 and 0.49 $g g^{-1}$, respectively.

These amorphous nanoporous N-doped carbons were then used to prepare composites via IWI with 10, 15, and 20 wt.% of LiCl, resulting in a homogeneous dispersion of salt nanoparticles inside micropores and mesopores, and remarkable adsorption heats were determined, reaching values above 2000 kJ kg^{-1} at 30°C and 12.5 mbar of water vapor pressure for composites containing 20 wt.% LiCl. In addition, the composites with 20 wt.% LiCl showed no deliquescence, no leakage, and excellent stability, as they preserved water uptake over 50 adsorption–desorption cycles at 30°C and 40% RH due to beneficial disordered hierarchical micro/mesoporous carbon matrices. The desorption (charging) step was performed at 120°C, a temperature achievable by evacuated tube collectors, demonstrating the potential of these composites for domestic low-temperature TCHS applications.

Acknowledgments

The authors thank Edi Kranjc for PXRD measurements, Mojca Opresnik for SEM images, Fabrizia Giordano for assistance with STA measurements, Dr. Ivan Jerman for Raman spectroscopy measurements, and Dr. Ana Kraš for FTIR measurements. The authors acknowledge the financial support of the Slovenian Research and Innovation Agency through the Research program Nanoporous Materials (P1-0021). Part of this research (determination of heat storage and thermophysical properties) was carried out within the RISEnergy project, which received funding from the European Union's Horizon Europe research and innovation program under Grant Agreement No 101131793.

Conflicts of Interest

The authors declare no conflicts of interest.

References

1. Z. Zeng, B. Zhao, and R. Wang, "Water Based Adsorption Thermal Battery: Sorption Mechanisms and Applications," *Energy Storage Materials* 54 (2023): 794–821.

2. Z. Y. Zeng, B. C. Zhao, and R. Z. Wang, "Passive Day and Night Heating for Zero Energy Buildings With Solar-Based Adsorption Thermal Battery," *Cell Reports Physical Science* 2, no. 9 (2021): 100578.

3. A. Ristić, "Sorption Material Developments for TES Applications," in *Advances in Energy Storage: Latest Developments From R&D to the Market*, ed. A. Hauer (John Wiley & Sons, 2022).

4. S. P. Casey, J. Elvins, S. Riffat, and A. Robinson, "Salt Impregnated Desiccant Matrices for 'Open' Thermochemical Energy Storage—Selection, Synthesis and Characterisation of Candidate Materials," *Energy and Buildings* 84 (2014): 412–425.

5. M. Abdullah, M. Koushaeian, N. A. Shah, and J. D. Chung, "A Review on Thermochemical Seasonal Solar Energy Storage Materials and Modeling Methods," *International Journal of Air-Conditioning and Refrigeration* 32, no. 1 (2024): 1.

6. A. Frazzica, V. Brancato, A. Caprì, C. Cannilla, L. G. Gordeeva, and Y. I. Aristov, "Development of 'Salt in Porous Matrix' Composites Based on LiCl for Sorption Thermal Energy Storage," *Energy* 208 (2020): 118338.

7. A. D. Grekova, L. G. Gordeeva, Z. Lu, R. Wang, and Y. I. Aristov, "Composite 'LiCl/MWCNT' as Advanced Water Sorbent for Thermal Energy Storage: Sorption Dynamics," *Solar Energy Materials and Solar Cells* 176 (2018): 273–279.

8. B. Lian, S. De Luca, Y. You, et al., "Extraordinary Water Adsorption Characteristics of Graphene Oxide," *Chemical Science* 9, no. 22 (2018): 5106–5111.

9. W. Li, J. J. Klemeš, Q. Wang, and M. Zeng, "Development and Characteristics Analysis of Salt-Hydrate Based Composite Sorbent for Low-Grade Thermochemical Energy Storage," *Renewable Energy* 157 (2020): 920–940.

10. T. Yan, T. Li, J. Xu, et al., "Ultrahigh-Energy-Density Sorption Thermal Battery Enabled by Graphene Aerogel-Based Composite Sorbents for Thermal Energy Harvesting From Air," *ACS Energy Letters* 6, no. 5 (2021): 1795–1802.

11. X. Yang, S. Li, J. Zhao, H. Huang, and L. Deng, "Fabrication of LiOH-Metal Organic Framework Derived Hierarchical Porous Host Carbon Matrix Composites for Seasonal Thermochemical Energy Storage," *Nano Research* 15, no. 9 (2022): 8028–8038.

12. W. Chaikittisilp, M. Hu, H. Wang, et al., "Nanoporous Carbons Through Direct Carbonization of a Zeolitic Imidazolate Framework for Supercapacitor Electrodes," *Chemical Communications* 48, no. 58 (2012): 7259–7261.

13. M. Yuan, M. Gao, Q. Shi, and J. Dong, "Understanding the Characteristics of Water Adsorption in Zeolitic Imidazolate Framework-Derived Porous Carbon Materials," *Chemical Engineering Journal* 379 (2020): 122412.

14. J. Marčec, A. Ristić, and N. Z. Logar, "New Insights Into ZIF-90 Synthesis," *Molecules* 29, no. 16 (2024): 3731.

15. J. Serafin, B. Dziejarski, O. F. Cruz Junior, and J. Sreńscek-Nazzal, "Design of Highly Microporous Activated Carbons Based on Walnut Shell Biomass for H_2 and CO_2 Storage," *Carbon* 201 (2023): 633–647.

16. X. Liu, J. Choi, Z. Xu, C. P. Grey, S. Fleischmann, and A. C. Forse, "Raman Spectroscopy Measurements Support Disorder-Driven Capacitance in Nanoporous Carbons," *Journal of the American Chemical Society* 146, no. 45 (2024): 30748–30752.

17. M. Ayiania, E. Weiss-Hortala, M. Smith, J.-S. McEwen, and M. Garcia-Perez, "Microstructural Analysis of Nitrogen-Doped Char by Raman Spectroscopy: Raman Shift Analysis From First Principles," *Carbon* 167 (2020): 559–574.

18. A. C. Ferrari and J. Robertson, "Interpretation of Raman Spectra of Disordered and Amorphous Carbon," *Physical Review B* 61, no. 20 (2000): 14095–14107.

19. S. Gautam, J. S. Sidhu, and M. Verma, "Influence of Reduction Duration on Reduced Graphene Oxide for Supercapacitor Energy Storage Enhancement," *Carbon Trends* 19 (2025): 100499.

20. A. Aijaz, N. Fujiwara, and Q. Xu, "From Metal–Organic Framework to Nitrogen-Decorated Nanoporous Carbons: High CO_2 Uptake and Efficient Catalytic Oxygen Reduction," *Journal of the American Chemical Society* 136, no. 19 (2014): 6790–6793.

21. J. Garcia-Martinez, C. Xiao, K. A. Cychosz, et al., "Evidence of Intracrystalline Mesostructured Porosity in Zeolites by Advanced Gas Sorption, Electron Tomography and Rotation Electron Diffraction," *ChemCatChem* 6, no. 11 (2014): 3110–3115.

22. L. H. Wee, M. Meledina, S. Turner, et al., "1D-2D-3D Transformation Synthesis of Hierarchical Metal–Organic Framework Adsorbent for Multicomponent Alkane Separation," *Journal of the American Chemical Society* 139, no. 2 (2017): 819–828.

23. R. Li, X. Han, Q. Liu, et al., "Porous Carbon Materials With Improved Hydrogen Storage Capacity by Carbonizing Zn(BDC)$TED_{0.5}$," *Journal of Solid State Chemistry* 314 (2022): 123409.

24. M. Thommes, K. Kaneko, A. V. Neimark, et al., "Physisorption of Gases, With Special Reference to the Evaluation of Surface Area and Pore Size Distribution (IUPAC Technical Report)," *Pure and Applied Chemistry* 87, no. 9–10 (2015): 1051–1069.

25. P. Shang, M. Liu, Y. Mei, et al., "Urea-Mediated Monoliths Made of Nitrogen-Enriched Mesoporous Carbon Nanosheets for High-Performance Aqueous Zinc Ion Hybrid Capacitors," *Small* 18, no. 16 (2022): 2108057.

26. A. V. Neimark, Y. Lin, P. I. Ravikovitch, and M. Thommes, "Quenched Solid Density Functional Theory and Pore Size Analysis of Micro-Mesoporous Carbons," *Carbon* 47, no. 7 (2009): 1617–1628.

27. S. Cao, T. Chen, S. Zheng, Y. Bai, and H. Pang, "High-Performance Capacitive Deionization and Killing Microorganism in Surface-Water by ZIF-9 Derived Carbon Composites," *Small Methods* 5, no. 12 (2021): 2101070.

28. P. Zhang, F. Sun, Z. Xiang, et al., "ZIF-Derived In Situ Nitrogen-Doped Porous Carbons as Efficient Metal-Free Electrocatalysts for Oxygen Reduction Reaction," *Energy & Environmental Science* 7, no. 1 (2014): 442–450.

29. A. Ristić and N. Zabukovec Logar, "New Composite Water Sorbents $CaCl_2$-PHTS for Low-Temperature Sorption Heat Storage: Determination of Structural Properties," *Nanomaterials* 9, no. 1 (2018): 27.

30. L. Liu, S. Tan, T. Horikawa, D. D. Do, D. Nicholson, and J. Liu, "Water Adsorption on Carbon: A Review," *Advances in Colloid and Interface Science* 250 (2017): 64–78.

31. Y. Xiao, H. Yang, X. Bu, and P. Feng, "ZIF-8 Derived Carbon Materials With Multifunctional Selective Adsorption Abilities," *Carbon* 176 (2021): 421–430.

32. W.-H. Lin, Y.-L. Chen, S.-Y. Yang, et al., "Toward Enhanced Atmospheric Water Harvesting in Arid Conditions via Mixed-Ligand MOF-Derived Porous Carbon," *ACS Applied Materials & Interfaces* 17, no. 23 (2025): 34052–34062.

33. Y. Peng, Z. Chen, R. Zhang, et al., "Oxygen-Containing Functional Groups Regulating the Carbon/Electrolyte Interfacial Properties Toward Enhanced K^+ Storage," *Nano-Micro Letters* 13, no. 1 (2021): 192.

34. Y. Sun, A. Spieß, C. Jansen, et al., "Tunable LiCl@UiO-66 Composites for Water Sorption-Based Heat Transformation Applications," *Journal of Materials Chemistry A* 8, no. 26 (2020): 13364–13375.

35. W. Xu, Y. Wang, H. Xing, J. Peng, and Y. Luo, "Optimization of UiO-66/$CaCl_2$ Composite Material for Thermal Energy Storage," *Microporous and Mesoporous Materials* 355 (2023): 112574.

36. M. Ocvirk, A. Ristić, and N. Zabukovec Logar, "Synthesis of Mesoporous γ-Alumina Support for Water Composite Sorbents for Low Temperature Sorption Heat Storage," *Energies* 14, no. 22 (2021): 7809.

37. A. Frazzica, V. Brancato, V. Palomba, and S. Vasta, "Sorption Thermal Energy Storage," in *Recent Advancements in Materials and Systems for Thermal Energy Storage* (Springer, 2019).

38. D. G. Atinafu, W. Dong, C. Hou, et al., "A Facile One-Step Synthesis of Porous N-Doped Carbon From MOF for Efficient Thermal Energy Storage Capacity of Shape-Stabilized Phase Change Materials," *Materials Today Energy* 12 (2019): 239–249.

39. X. Yang, S. Li, J. Zhao, X. Wang, H. Huang, and Y. Wang, "Construction of Metal Organic Framework-Derived Hollow-Structured Mesoporous Carbon Based Lithium Hydroxide Composites for Low-Grade Thermal Energy Storage," *Composites, Part B: Engineering* 232 (2022): 109604.

40. J. Canivet, J. Bonnefoy, C. Daniel, A. Legrand, B. Coasne, and D. Farrusseng, "Structure–Property Relationships of Water Adsorption in Metal–Organic Frameworks," *New Journal of Chemistry* 38, no. 7 (2014): 3102–3111.

41. M. Gao, J. Wang, Z. Rong, Q. Shi, and J. Dong, "A Combined Experimental-Computational Investigation on Water Adsorption in Various ZIFs With the SOD and RHO Topologies," *RSC Advances* 8, no. 69 (2018): 39627–39634.

42. J. Kossmann, R. Rothe, T. Heil, M. Antonietti, and N. López-Salas, "Ultrahigh Water Sorption on Highly Nitrogen Doped Carbonaceous Materials Derived From Uric Acid," *Journal of Colloid and Interface Science* 602 (2021): 880–888.

43. T. Horikawa, N. Sakao, and D. D. Do, "Effects of Temperature on Water Adsorption on Controlled Microporous and Mesoporous Carbonaceous Solids," *Carbon* 56 (2013): 183–192.

44. I. Lamata-Bermejo, W. Keil, K. Nolkemper, et al., "Understanding the Wettability of C_1N_1 (Sub)Nanopores: Implications for Porous Carbonaceous Electrodes," *Angewandte Chemie International Edition* 63, no. 50 (2024): e202411493.

45. W.-H. Lin, Y.-L. Chen, S.-Y. Yang, et al., "Toward Enhanced Atmospheric Water Harvesting in Arid Conditions via Mixed-Ligand MOF-Derived Porous Carbon," *ACS Applied Materials & Interfaces* 17, no. 23 (2025): 34052–34062.

46. K. V. Kumar, K. Preuss, Z. X. Guo, and M. M. Titirici, "Understanding the Hydrophilicity and Water Adsorption Behavior of Nanoporous Nitrogen-Doped Carbons," *Journal of Physical Chemistry C* 120, no. 32 (2016): 18167–18179.

47. H.-J. Wang, A. Kleinhammes, T. P. McNicholas, J. Liu, and Y. Wu, "Water Adsorption in Nanoporous Carbon Characterized by In Situ NMR: Measurements of Pore Size and Pore Size Distribution," *Journal of Physical Chemistry C* 118, no. 16 (2014): 8474–8480.

48. T. Matsuoka, H. Hatori, M. Kodama, J. Yamashita, and N. Miyajima, "Capillary Condensation of Water in the Mesopores of Nitrogen-Enriched Carbon Aerogels," *Carbon* 42, no. 11 (2004): 2346–2349.

49. J.-H. Feng, F. Lu, Z. Chen, et al., "Rapid Solar-Driven Atmospheric Water-Harvesting With MAF-4-Derived Nitrogen-Doped Nanoporous Carbon," *Chemical Science* 15, no. 25 (2024): 9557–9565.

50. V. A. Cardozo–Mata, J. A. Pescador–Rojas, A. Hernández–Hernández, et al., "Chemical Interaction Between Nitrogen-Doped Graphene Defects and a Copper (111) Surface: Effects on Water Molecule Adsorption," *Applied Surface Science* 502 (2020): 144149.

51. F. Zheng, Y. Yang, and Q. Chen, "High Lithium Anodic Performance of Highly Nitrogen-Doped Porous Carbon Prepared From a Metal-Organic Framework," *Nature Communications* 5 (2014): 5261.

52. N. Qiang, T. Shi, T. Liu, Y. Cao, H. Miu, and J. He, "A Novel Analytical Method for the In-Depth Study of the Effects of Humidity and Temperature on the Adsorption of Volatile Organic Compounds," *IOP Conference Series: Earth and Environmental Science* 295 (2019): 012033.

53. X. Sun, T. Wu, Z. Yan, et al., "Novel MOF-5 Derived Porous Carbons as Excellent Adsorption Materials for n-Hexane," *Journal of Solid State Chemistry* 271 (2019): 354–360.

54. D. Jeong, S. C. Kim, T. An, et al., "Synthesis of Aluminum-Based Metal–Organic Framework (MOF)-Derived Carbon Nanomaterials and Their Water Adsorption Isotherm," *Nanomaterials* 13, no. 16 (2023): 2351.

55. C. Wang, H. Yin, P. Tian, et al., "Remarkable Adsorption Performance of MOF-199 Derived Porous Carbons for Benzene Vapor," *Environmental Research* 184 (2020): 109323.

56. A. C. Forse, C. Merlet, C. P. Grey, and J. M. Griffin, "NMR Studies of Adsorption and Diffusion in Porous Carbonaceous Materials," *Progress in Nuclear Magnetic Resonance Spectroscopy* 124–125 (2021): 57–84.

57. A. C. Forse, J. M. Griffin, V. Presser, Y. Gogotsi, and C. P. Grey, "Ring Current Effects: Factors Affecting the NMR Chemical Shift of Molecules Adsorbed on Porous Carbons," *Journal of Physical Chemistry C* 118, no. 14 (2014): 7508–7514.

58. T. K. Das, S. Banerjee, M. Pandey, B. Vishwanadh, R. J. Kshirsagar, and V. Sudarsan, "Effect of Surface Functional Groups on Hydrogen Adsorption Properties of Pd Dispersed Reduced Graphene Oxide," *International Journal of Hydrogen Energy* 42, no. 12 (2017): 8032–8041.

59. A. R. Ambrozio, T. R. Lopes, D. F. Cipriano, F. Souza, W. L. Scopel, and J. Freitas, "Combined Experimental and Computational ^{1}H NMR Study of Water Adsorption Onto Graphenic Materials," *Journal of Magnetic Resonance Open* 14–15 (2023): 100091.

60. L. Cervini, O. D. Lynes, G. R. Akien, A. Kerridge, N. S. Barrow, and J. M. Griffin, "Factors Affecting the Nucleus-Independent Chemical Shift in NMR Studies of Microporous Carbon Electrode Materials," *Energy Storage Materials* 21 (2019): 335–346.

61. J. Xu, T. Li, J. Chao, et al., "Efficient Solar-Driven Water Harvesting From Arid Air With Metal–Organic Frameworks Modified by Hygroscopic Salt," *Angewandte Chemie International Edition* 59, no. 13 (2020): 5202–5210.

62. S. Bennici, P. Dutournié, J. Cathalan, et al., "Heat Storage: Hydration Investigation of $MgSO_4$/Active Carbon Composites, From Material Development to Domestic Applications Scenarios," *Renewable and Sustainable Energy Reviews* 158 (2022): 112197.

63. V. Brancato, L. G. Gordeeva, A. D. Grekova, et al., "Water Adsorption Equilibrium and Dynamics of LiCL/MWCNT/PVA Composite for Adsorptive Heat Storage," *Solar Energy Materials and Solar Cells* 193 (2019): 133–140.

64. J. Lin, Q. Zhao, H. Huang, H. Mao, Y. Liu, and Y. Xiao, "Applications of Low-Temperature Thermochemical Energy Storage Systems for Salt Hydrates Based on Material Classification: A Review," *Solar Energy* 214 (2021): 149–178.

65. S. K. Henninger, F. Jeremias, H. Kummer, P. Schossig, and H.-M. Henning, "Novel Sorption Materials for Solar Heating and Cooling," *Energy Procedia* 30 (2012): 279–288.

Supporting Information

Additional supporting information can be found online in the Supporting Information section.
Supporting File: cey270256-sup-0001-Supporting_Information.